Light-sheet generation in inhomogeneous media using self-reconstructing beams and the STED-principle

Cristian Gohn-Kreuz and Alexander Rohrbach[*]

Laboratory for Bio- and Nano-Photonics, Department of Microsystems Engineering—IMTEK, University of Freiburg, 79110 Freiburg, Germany
[*]*rohrbach@imtek.uni-freiburg.de*

Abstract: Self-reconstruction of Bessel beams in inhomogeneous media is beneficial in light-sheet based microscopy. Although the beam's ring system enables propagation stability, the resulting image contrast is reduced. Here, we show that by a combination of two self-reconstructing beams with different orbital angular momenta it is possible to inhibit fluorescence from the ring system by using stimulated emission depletion (STED) even in strongly scattering media. Our theoretical study shows that the remaining fluorescence γ depends non-linearly on the beams' relative radial and orbital angular momenta. For various scattering media we demonstrate that γ remains remarkably stable over long beam propagation distances.

References and links

1. A. P. Mosk, A. Lagendijk, G. Lerosey, and M. Fink, "Controlling waves in space and time for imaging and focusing in complex media," Nat. Photonics **6**(5), 283–292 (2012).
2. Y. Choi, T. D. Yang, C. Fang-Yen, P. Kang, K. J. Lee, R. R. Dasari, M. S. Feld, and W. Choi, "Overcoming the diffraction limit using multiple light scattering in a highly disordered medium," Phys. Rev. Lett. **107**(2), 023902 (2011).
3. F. O. Fahrbach, P. Simon, and A. Rohrbach, "Microscopy with self-reconstructing beams," Nat. Photonics **4**(11), 780–785 (2010).
4. P. J. Keller, A. D. Schmidt, J. Wittbrodt, and E. H. K. Stelzer, "Reconstruction of zebrafish early embryonic development by scanned light sheet microscopy," Science **322**(5904), 1065–1069 (2008).
5. T. A. Planchon, L. Gao, D. E. Milkie, M. W. Davidson, J. A. Galbraith, C. G. Galbraith, and E. Betzig, "Rapid three-dimensional isotropic imaging of living cells using Bessel beam plane illumination," Nat. Methods **8**(5), 417–423 (2011).
6. F. O. Fahrbach and A. Rohrbach, "Propagation stability of self-reconstructing Bessel beams enables contrast-enhanced imaging in thick media," Nat. Commun. **3**, 632 (2012).
7. S. W. Hell, "Strategy for far-field optical imaging and writing without diffraction limit," Phys. Lett. A **326**(1-2), 140–145 (2004).
8. S. Berning, K. I. Willig, H. Steffens, P. Dibaj, and S. W. Hell, "Nanoscopy in a living mouse brain," Science **335**(6068), 551 (2012).
9. E. Baumgart and U. Kubitscheck, "Scanned light sheet microscopy with confocal slit detection," Opt. Express **20**(19), 21805–21814 (2012).
10. L. Silvestri, A. Bria, L. Sacconi, G. Iannello, and F. S. Pavone, "Confocal light sheet microscopy: micron-scale neuroanatomy of the entire mouse brain," Opt. Express **20**(18), 20582–20598 (2012).
11. P. J. Keller, A. D. Schmidt, A. Santella, K. Khairy, Z. Bao, J. Wittbrodt, and E. H. K. Stelzer, "Fast, high-contrast imaging of animal development with scanned light sheet-based structured-illumination microscopy," Nat. Methods **7**(8), 637–642 (2010).
12. J. Mertz, "Optical sectioning microscopy with planar or structured illumination," Nat. Methods **8**(10), 811–819 (2011).

13. L. Gao, L. Shao, C. D. Higgins, J. S. Poulton, M. Peifer, M. W. Davidson, X. Wu, B. Goldstein, and E. Betzig, "Noninvasive imaging beyond the diffraction limit of 3D dynamics in thickly fluorescent specimens," Cell **151**(6), 1370–1385 (2012).
14. B.-C. Chen, W. R. Legant, K. Wang, L. Shao, D. E. Milkie, M. W. Davidson, C. Janetopoulos, X. S. Wu, J. A. Hammer 3rd, Z. Liu, B. P. English, Y. Mimori-Kiyosue, D. P. Romero, A. T. Ritter, J. Lippincott-Schwartz, L. Fritz-Laylin, R. D. Mullins, D. M. Mitchell, J. N. Bembenek, A.-C. Reymann, R. Böhme, S. W. Grill, J. T. Wang, G. Seydoux, U. S. Tulu, D. P. Kiehart, and E. Betzig, "Lattice light-sheet microscopy: Imaging molecules to embryos at high spatiotemporal resolution," Science **346**(6208), 1257998 (2014).
15. J. Palero, S. I. Santos, D. Artigas, and P. Loza-Alvarez, "A simple scanless two-photon fluorescence microscope using selective plane illumination," Opt. Express **18**(8), 8491–8498 (2010).
16. T. V. Truong, W. Supatto, D. S. Koos, J. M. Choi, and S. E. Fraser, "Deep and fast live imaging with two-photon scanned light-sheet microscopy," Nat. Methods **8**(9), 757–760 (2011).
17. F. O. Fahrbach, V. Gurchenkov, K. Alessandri, P. Nassoy, and A. Rohrbach, "Light-sheet microscopy in thick media using scanned Bessel beams and two-photon fluorescence excitation," Opt. Express **21**(11), 13824–13839 (2013).
18. M. Friedrich, Q. Gan, V. Ermolayev, and G. S. Harms, "STED-SPIM: stimulated emission depletion improves sheet illumination microscopy resolution," Biophys. J. **100**(8), L43–L45 (2011).
19. T. Scheul, I. Wang, and J.-C. Vial, "STED-SPIM made simple," Opt. Express **22**(25), 30852–30864 (2014).
20. P. Zhang, P. M. Goodwin, and J. H. Werner, "Fast, super resolution imaging via Bessel-beam stimulated emission depletion microscopy," Opt. Express **22**(10), 12398–12409 (2014).
21. M. Leutenegger, C. Eggeling, and S. W. Hell, "Analytical description of STED microscopy performance," Opt. Express **18**(25), 26417–26429 (2010).
22. X. Chu and W. Wen, "Quantitative description of the self-healing ability of a beam," Opt. Express **22**(6), 6899–6904 (2014).
23. F. O. Fahrbach, V. Gurchenkov, K. Alessandri, P. Nassoy, and A. Rohrbach, "Self-reconstructing sectioned Bessel beams offer submicron optical sectioning for large fields of view in light-sheet microscopy," Opt. Express **21**(9), 11425–11440 (2013).
24. V. Jarutis, R. Paškauskas, and A. Stabinis, "Focusing of Laguerre–Gaussian beams by axicon," Opt. Commun. **184**(1-4), 105–112 (2000).
25. It is interesting to note, that for $k_0 NA \cdot w \gg 1$, which holds true for all reasonable beam parameters, the axial position of the peak intensities $z_{max} = 0.5 \cdot w \cdot n/NA$ of the Bessel beams is independent of the orbital angular momentum $\hbar \ell$. This is not true for other means of generating higher order Bessel beams, for example by focusing a higher-order Laguerre-Gauss beam with a regular axicon lens [24,31].
26. J. Arlt and K. Dholakia, "Generation of high-order Bessel beams by use of an axicon," Opt. Commun. **177**(1-6), 297–301 (2000).
27. G. Vicidomini, G. Moneron, C. Eggeling, E. Rittweger, and S. W. Hell, "STED with wavelengths closer to the emission maximum," Opt. Express **20**(5), 5225–5236 (2012).
28. G. H. Patterson, S. M. Knobel, W. D. Sharif, S. R. Kain, and D. W. Piston, "Use of the green fluorescent protein and its mutants in quantitative fluorescence microscopy," Biophys. J. **73**(5), 2782–2790 (1997).
29. E. Rittweger, B. R. Rankin, V. Westphal, and S. W. Hell, "Fluorescence depletion mechanisms in super-resolving STED microscopy," Chem. Phys. Lett. **442**(4-6), 483–487 (2007).
30. A. Esposito, C. P. Dohm, M. Bähr, and F. S. Wouters, "Unsupervised fluorescence lifetime imaging microscopy for high content and high throughput screening," Mol. Cell. Proteomics **6**(8), 1446–1454 (2007).
31. A. Rohrbach, "Artifacts resulting from imaging in scattering media: a theoretical prediction," Opt. Lett. **34**(19), 3041–3043 (2009).

1. Introduction

The probability to induce nonlinear optical processes such as multi-harmonic generation or multi-photon excitation but also stimulated emission depends on the quantum state of an atom or molecule. But, it also depends on the intensity of the light interacting with that molecule. The phase delay between individual photons that hit the molecule's interaction cross-section defines the interference intensity and thereby the interaction probability. The relative photon phases $\delta\phi(\mathbf{r})$ depend on their state of coherence, but also on the relative linear and orbital angular momentum between the photons, $\delta\hbar\mathbf{k}(\mathbf{r}) = \hbar\delta[\nabla\phi(\mathbf{r})]$ and $\Delta\hbar l$. Thereby, the correlations in momentum and phase between the many photons propagating through a large scattering medium determine the space-variant interactions between photons and molecules inside the large object [1,2]. These spatial variations have a strong impact especially on modern light microscopy techniques.

It could be shown, that the initial phase profile of a laser beam with confined linear radial momentum increases the beam's penetration depth in a strongly scattering medium [3]. In

other words, the initial distribution of phase and momentum determines the ratio of ballistic and diffusive photons while propagating through large dielectric media. This unexpected effect led to an improvement of light-sheet based (LSB) microscopes, where slightly focused laser beams illuminate only that part of the object, which is in the focal plane of an imaging system [3,4]. The ultimate goal of these LSB microscopes is to generate a light sheet as thin as possible that penetrates as deep as possible into large biological samples without significant beam spreading and scattering.

The usage of self-reconstructing beams with narrow-band radial momentum, such as Bessel beams, enables high penetration depths and large depths of field at relatively high numerical apertures. However, due to their inherent extended ring system, which transports self-healing photons, image contrast is reduced in line-scanning LSB-microscopy [5,6]. A completely different technique, STED, uses stimulated emission to enable super-resolution in point scanning microscopy by depleting unwanted excited fluorophores [7,8] very locally around the center of the focus. A combination of both techniques, microscopy with self-reconstructing beams (MISERB) and STED-microscopy both in line-scanning mode, could enable ultra-thin light sheets even in thick scattering media. The realization of such a combination would require that first both the fluorescence excitation beam and the fluorescence depletion beam (STED beam) exhibit self-reconstructing capabilities in inhomogeneous media. Second, their difference in radial and orbital angular photon momentum, $\Delta \hbar k_r$ and $\Delta \hbar l$, must be matched such that the depletion efficiency is optimal and remains approximately propagation invariant despite significant scattering and loss in the photons' phase correlation.

Other techniques to increase the contrast in light sheet based microscopy are the use of a line confocal pinhole in the detection path [6,9,10], structured illumination [5,11–14] or the use of multi-photon excitation [15–17]. Compared to these techniques the combination of Bessel beam light sheet microscopy and the STED principle enables the realization of potentially arbitrarily thin light sheets and thus arbitrarily high contrast and resolution perpendicular to the image plane, while still profiting from the increased penetration depth of Bessel beam illumination [3]. Unlike with structured illumination there is no need to record multiple raw frames per image, which makes this technique faster and eliminates the need for any post processing. It is furthermore less cost-intensive than two-photon excitation and despite the lower excitation and depletion wavelengths it also potentially less photo-toxic. This is due to the fact the light intensities involved in STED microscopy are up to 3 orders of magnitude smaller than the ones involved in two-photon microscopy.

Among the few studies that investigate the combination of light sheet microscopy with the STED [18–20] principle, only one theoretical study [20] investigates a static Bessel beam in an ideal, non-scattering environment and the depletion of the Bessel ring system.

In this paper we investigate theoretically and by computer simulations the relation between the radial and orbital angular momentum of the excitation beam and the depletion beam optimizing the depletion beam pattern in light sheet based microscopy with Bessel beam illumination. In this context, we investigate the stability of the depletion in strongly scattering media and show that it is possible to form superior light sheets using this illumination scheme compared to conventional Bessel or Gaussian beam illumination.

2. The STED-MISERB principle

The combination of these two microscopy techniques requires a phase shaping element that generates two different self-reconstructing beams, which are characterized by a very narrow radial angular spectrum. The first beam excites fluorescence proportional to its illumination intensity $I_{EX}(r,\varphi,z) = |E_{EX}(r,\varphi,z)|^2$ which, in the ideal case, is a 0-th order Bessel beam with electric field $E_{EX}(r,\varphi,z) = A_{EX} \cdot J_0(k_r r) \cdot \exp(ik_z z)$. The second beam depletes the fluorescence excited in the sample by stimulated emission except for a defined area in the beam center, where the beam intensity $I_{ST}(r,\varphi,z) = |E_{ST}(r,\varphi,z)|^2$ must drop to zero by destructive interference. This can be achieved by a Bessel beam of order $l \neq 0$ and field $E_{ST}(r,\varphi) = A_{ST} \cdot J_\ell(\alpha k_r r) \cdot \exp[i(\ell\varphi + k_z z)]$, which has a non-zero orbital angular momentum in addition to the narrow- band radial linear momentum.
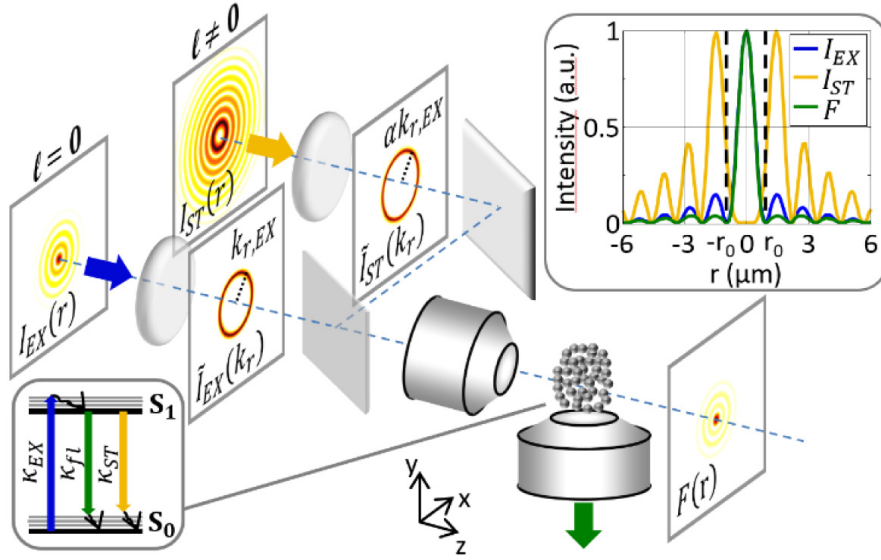
Fig. 1. Schematic of STED-MISERB principle. The excitation beam and the depletion beam, with intensities $I_{EX}(r)$ and $I_{ST}(r)$, differ in angular momentum ℏl and radial momentum ℏkr. The resulting fluorescence F(r) is a long thin light needle.

The angular spectra, i.e. the lateral Fourier transforms of the beams' fields, are δ-ring shaped:

$$\begin{aligned}
\tilde{E}_{EX}(k_r,\tilde{\varphi}) &= \tilde{E}_{0EX} \cdot \delta(k_0 NA - k_r) \\
\tilde{E}_{ST}(k_r,\tilde{\varphi}) &= \tilde{E}_{0ST} \cdot \delta(\alpha k_0 NA - k_r) \cdot e^{i\ell\tilde{\varphi}}
\end{aligned} \tag{1}$$

The radial linear momentum scales with $k_0 \cdot NA = 2\pi/\lambda \cdot n \cdot \sin\theta$ and is further enhanced by a factor α for the STED beam, corresponding to potentially different NAs of the excitation and the STED beam respectively. Figure 1 shows the schematic of the STED-MISERB setup, where both beams are displayed by their intensities in position space $I(r)$ and by their ring-like power spectra in reciprocal Fourier space $\tilde{I}(k_r)$. After combining the beams by a beam splitter, both beams propagate through a cluster of dielectric spheres, which are embedded in a fluorescing gel and serve as a model system for a scattering medium. During propagation, both beams are multiply scattered at the spheres, such that the intensity of each beam is characterized by interference patterns that become the less correlated to the initial profile the longer the beams propagate.

The resulting fluorescence $F(\mathbf{r}) \approx C_{ext}(\mathbf{r}) \cdot Q_{fl} \cdot \eta(\mathbf{r}) \cdot I_{EX}(\mathbf{r})$ is approximately proportional to the extinction cross-section $C_{ext}(\mathbf{r})$ and the quantum efficiency Q_{fl} of the fluorophores, to the excitation intensity $I_{EX}(\mathbf{r})$ and the probability for spontaneous emission $\eta(\mathbf{r})$. A useful expression for this space-variant distribution is $\eta(\mathrm{r}) = \mathrm{I}_{sat} / (\mathrm{I}_{sat} + \mathrm{I}_{ST}(\mathrm{r}))$ [21], which depends on the intensity of the STED beam $I_{ST}(\mathbf{r})$ and the saturation intensity $I_{sat} = (\mathrm{hc} \cdot k_{fl}) / (\sigma_{STED} \lambda_{STED})$ at which the rates of depletion and fluorescence equal each other, $\kappa_{ST} = \kappa_{fl}$ (see inset of Fig. 1).

3. The optimal STED beam in the non-scattering case

In a first step we aim to determine the optimal focusing of the STED beam relative to the excitation beam, i.e. we seek the optimal ratio of radial momentum $\alpha = (\hbar k_{r,ST}) / (\hbar k_{r,EX})$ and the optimal angular momentum $\hbar \ell$ of the depletion beam in the absence of scatterers. In order to make STED-MISERB as energy efficient as possible and to minimize bleaching and potential photodamage, the overlap of the depletion beam with the excitation beam should be maximal in the ring system of the excitation beam and minimal in its center. The overlap between both beams, which differ in their phases through ℓ and α, can be quantified by the normalized cross correlation coefficient of the corresponding intensity distributions [22]:

$$\rho(\ell, \alpha) = \frac{1}{\sqrt{A}} \cdot \int_{r_{in}}^{r_{out}} I_{EX}(\mathrm{r}') \cdot I_{ST}(\mathrm{r}', \ell, \alpha) \, \mathrm{r}' \, \mathrm{dr}' \tag{2}$$

Here $A = \int_{r_{in}}^{r_{out}} I_{EX}^2(\mathrm{r}') \mathrm{r}' \mathrm{dr}' \cdot \int_{r_{in}}^{r_{out}} I_{ST}^2(\mathrm{r}') \mathrm{r}' \mathrm{dr}'$ is a normalization term. The beam overlap in the ring system ρ_{ring} is obtained by integration from the inner radius $r_{in} = r_0$ to the outer radius $r_{out} \to \infty$, whereas ρ_{cent} is obtained by integration from $r_{in} = 0$ to $r_{out} \to r_0$. $r_0 = 2.4048 \cdot k_{r,EX}^{-1}$, the first root of the Bessel beam, is chosen as the radius discriminating the center region from the ring system (see inset of Fig. 1). The beam overlap is optimized if $\rho_{diff} = \rho_{ring} - \rho_{cent}$ becomes maximal for all relative linear radial momenta α and orbital angular momenta ℓ being experimentally relevant.

The effect of the depletion beam on the resulting fluorescence distribution is quantified by the spatial fluorescence ratio $\overline{F}(\ell, \alpha)$, which is defined by the integrated fluorescence in the central beam region [23] relative to the integrated fluorescence in the ring system:

$$\overline{F}(\ell, \alpha) = \frac{\iint_{\sqrt{x^2+y^2} < r_0} F(\mathrm{x}, \mathrm{y}, \ell, \alpha) \, \mathrm{dxdy}}{\iint_{\sqrt{x^2+y^2} \geq r_0} F(\mathrm{x}, \mathrm{y}, \ell, \alpha) \, \mathrm{dxdy}} \tag{3}$$

Since the fluorescence distribution $F(r, I_{ST}(r))$ strongly depends on the STED intensity $I_{ST}(r)$, this ratio also strongly depends on $I_{ST}(r)$. The spatial fluorescence enhancement $\gamma(\ell, \alpha)$ due to the depletion by the STED beam is defined as:

$$\gamma(\ell, \alpha) = \frac{\overline{F}(\mathrm{I}_{ST} > 0, \ell, \alpha)}{\overline{F}(\mathrm{I}_{ST} = 0, \ell, \alpha)} \tag{4}$$

In order to find the optimal momenta α_{opt} and ℓ_{opt}, the ratio $\gamma(\ell, \alpha)$ needs to be maximized too.

As ideal Bessel beams contain an infinite amount of energy, we approximate the ideal Bessel beam by a focused Gaussian beam with conical phase profile. In order to generate a Bessel beam of order ℓ, the conical phase is modulated with an azimuthal phase $\phi(\mathrm{r}, \varphi) = \mathrm{k}_o \, NA \cdot r + \ell \varphi$, which can easily be realized with a spatial light modulator. The field magnitudes of the incident Gaussian beams are $\exp(-\mathrm{r}^2 / w_{EX}^2)$ and $\exp(-\mathrm{r}^2 / w_{ST}^2)$ for the

excitation and depletion beam, respectively. The beam widths w are adapted such that the resulting Bessel beams are of equal lengths, $L_{FWHM} \approx 0.8 w_{EX} n / NA_{EX} \approx 0.8 w_{ST} n / NA_{ST}$, where n is the refractive index of the propagation medium [24–26].

In order to perform our study as close as possible to potential experiments, we used an excitation wavelength of $\lambda_{EX} = 488nm$ in water ($n = 1.33$) and a depletion wavelength of $\lambda_{ST} = 560nm$ [27] for the numerical evaluation of the beam overlap ρ_{diff} and the enhancement of the fluorescence ratio $\gamma(\ell, \alpha)$. The fluorophore parameters $\sigma_{EX} \approx 2.3 \cdot 10^{-8} \mu m^2$; $\sigma_{ST} \approx 1.2 \cdot 10^{-8} \mu m^2$ and $\tau_{fl} = \kappa_{fl}^{-1} \approx 2.5ns$ were based on the green fluorescent protein (GFP) [28–30], resulting in a saturation intensity of $I_{sat} \approx 12mW / \mu m^2$. As shown in Fig. 2, the relative radial and orbital angular momenta between both beams could be optimized by maximizing the beam overlap and the spatial fluorescence enhancement within the momentum ranges $\hbar \ell$ with $\ell = 1 \dots 5$ and $\hbar k_{r,ST} = \hbar \alpha k_{r,EX}$ with $\alpha = 0.1 \dots 1.6$. The experimentally relevant parameters of the excitation beam were $\omega_{EX} = 10 \mu m$ and $k_{r,EX} = NA_{EX} \cdot 2\pi / \lambda_{EX}$ with $NA_{EX} = 0.25$. Figure 2(a) shows the beam overlap ρ_{diff}, which peaks for $\ell = 3, \alpha = 1.1$ (red curve) and $\ell = 4, \alpha = 1.3$ (cyan curve). The spatial fluorescence enhancement γ was analyzed for two typical STED powers P_{ST}. Figure 2(b) shows the results for $P_{ST} = 1W$, which can be easily achieved with a cw fiber laser. The optimal relative beam momenta in this case are $\ell = 3, \alpha = 1.1$ (red curve) and $\ell = 4, \alpha = 1.2$ (cyan curve), which fits very well to the momenta optimizing the beam overlap as shown in Fig. 2(a).
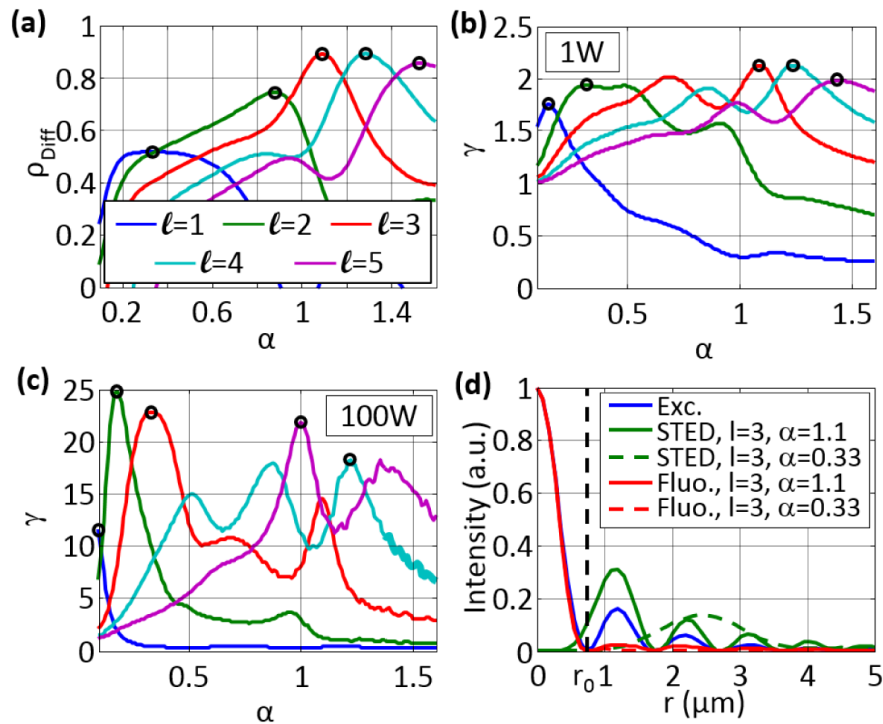
Fig. 2. Dependency of the beam overlap and the spatial fluorescence enhancement on the linear and angular beam momentum in STED-MISERB without scattering. (a) Beam overlap for $\ell = 1 \dots 5$ in dependence of α and fluorescence enhancement for laser powers (b) $P_{ST} = 1W$ and (c) $P_{ST} = 100W$. (d) Normalized beam profiles and resulting fluorescent signal for $P_{ST} = 1W, \ell = 3, \alpha = 1.1$ and $P_{ST} = 100W, \ell = 3, \alpha = 0.3$.

In a pulsed depletion scheme the peak power of the STED beam can easily reach $P_{ST} = 100W$ resulting in the γ distribution shown in Fig. 2(c). Here the optimal beam momenta give rise to even more pronounced γ-values at $\ell = 2, \alpha = 0.2$ (green curve) and $\ell = 3, \alpha = 0.3$ (red curve). The optimal relative radial momenta are smaller for higher P_{ST}, which per se results in a suboptimal beam overlap in the ring system (see Fig. 2(d)). This is however not required for an efficient depletion due to the high STED peak power. It is more important to keep the beam overlap in the center as small as possible in order to minimize the depletion in the center, which is possible with a small relative radial momentum α. Figure 2(d) displays the normalized beam profiles for the excitation and depletion beams as well as the resulting fluorescence distribution for both sets of beam momenta optimizing the fluorescence ratio. In both cases an efficient depletion of the ring system can be achieved, suppressing the peak fluorescence signal in the ring system to only 2.2% and 0.7% of the fluorescence signal in the center for $P_{ST} = 1W$ and $P_{ST} = 100W$, respectively.

4. The optimal STED beam in a strongly scattering medium

After having introduced the spatial fluorescence enhancement $\gamma(\ell, \alpha)$ to assess the STED quality for different orbital angular momenta l and relative radial momenta α, it is now the goal to test the stability of $\gamma(\ell, \alpha)$ during beam propagation through different strongly scattering media. The stability of $\gamma(\ell, \alpha)$ depends on the propagation stability of the excitation beam and the STED beam. The total fields $E_{EX}(x, y, z)$ and $E_{ST}(x, y, z)$ propagating through an inhomogeneous medium are calculated numerically using the beam propagation method [31]. This iterative method relies on a separation of the refractive index distribution $n(x, y, z)$ into a constant and space variant part $n(x, y, z) = n_{med} + \delta n(x, y, z)$. The simulation domain is divided in $N_x \times N_y \times N_z$ volume elements and the total fields of the excitation and the STED beam are computed iteratively in planes perpendicular to the propagation direction z, such that the fields in the plane z + dz are given by

$$E(x, y, z + dz) = \text{FT}^{-1}\left[\tilde{E}(k_x, k_y, z) \cdot e^{i\sqrt{k_0^2 n_{med}^2 - k_x^2 - k_y^2} \cdot dz} \right] \cdot e^{ik_0 \cdot \delta n(x,y,z) \cdot dz} \tag{5}$$

Here $FT^{-1}[..]$ denotes the inverse Fourier-Transform in x and y.
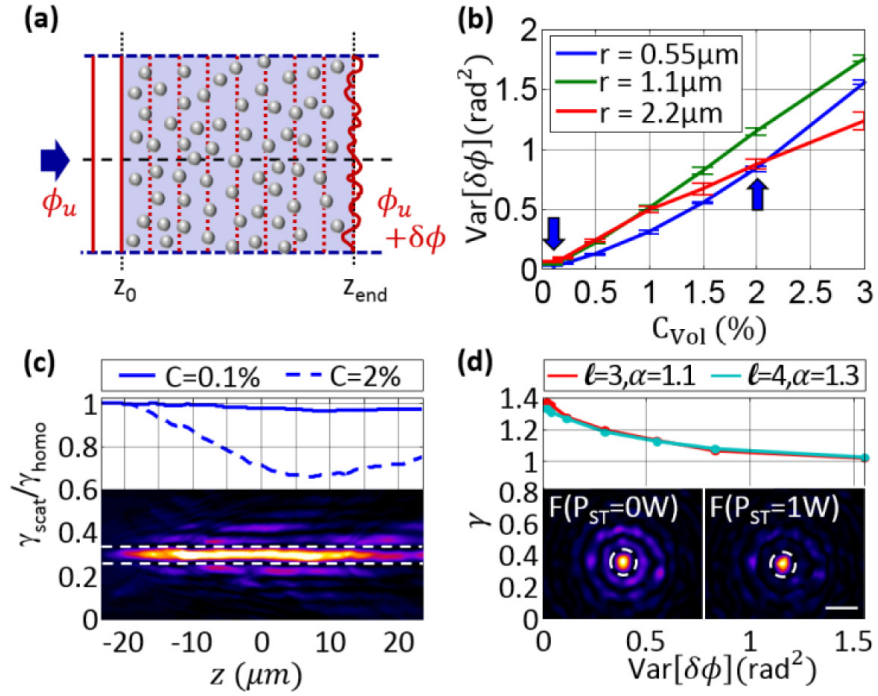
Fig. 3. Stability of the spatial fluorescence enhancement $\gamma(\ell,\alpha)$ upon propagation through different scattering media. (a) Distortion of a plane wavefront upon propagation through a scattering medium. (b) Variance of the scattering induced phase shift, averaged over 10 sample realizations. The error bar indicates the standard deviation. (c) Stability of the fluorescence enhancement factor upon propagation through two different sphere densities for a depletion beam with $P_{ST}=1W, \ell=3, \alpha=1.1$. The inset shows a slice through the excitation beam in a sample with Cvol = 2%. The dotted lines indicate the region $-r_0 \ldots r_0$, discriminating the center of the beam from the ring system. (d) Spatial fluorescence enhancement for different $\mathrm{Var}[\delta\phi]$ after propagation through the sphere clusters. The inset shows a xy slice through the fluorescence signal at z = 0µm for Cvol = 2%. The dotted circles indicate the center of the beams. The scale bar is 2µm.

To evaluate the propagation stability for inhomogeneous media with different scattering strength we introduce the variance of the phase shift $\delta\phi(x,y,z)$ after a specific propagation distance z as a measure. The quantity $\mathrm{Var}[\delta\phi(z)] = \sigma_{\delta\phi}^2(z)$

$$\mathrm{Var}[\delta\phi(z)] = \left\langle \left(\delta\phi(x,y,z) - \left\langle \delta\phi(x,y,z) \right\rangle \right)^2 \right\rangle = \frac{1}{r_{max}^2 \pi} \iint \left(\delta\phi(x,y,z) - \overline{\delta\phi}(z) \right)^2 dxdy \quad (6)$$

is calculated for a plane wave with field $\mathbf{E}_{pw}(\mathbf{r})$ propagating through a cluster of spheres. Here the symbol $\langle .. \rangle$ designates the average in x and y. Each scatterer induces a local phase delay on the wave front and thus increases $\delta\phi(x,y,z_{end}) = \arg\left(\mathbf{E}_{pw}(x,y,z_{end})\right) - \phi_i(x,y,z_{end})$ or $\mathrm{Var}[\delta\phi(z)]$, respectively. This is illustrated in Fig. 3(a). This measure allows the characterization of the scattering medium taking into consideration the change of the wavefront, which is crucial for coherent beam formation. Other measures as for example the scattering coefficient do not directly take this change into account.

After propagation through a cluster of spheres, $\mathrm{Var}[\delta\phi]$ increases with the volume concentration C_{Vol} of the dielectric spheres, or correspondingly with $\delta n(\mathrm{x,y,z}) = \delta n(C_{Vol})$. As shown in Fig. 3(b), the increase is nearly linear for both a plane wave and a superposition of plane waves such as a Bessel beam. $\mathrm{Var}[\delta\phi]$ in Fig. 3(b) was computed by averaging the

phase variance after propagation through ten clusters of spheres each with a different random bead distribution with the same concentration, bead size and refractive index. The clusters where 47 μm long and the beads with refractive index $n_s = 1.41$ were embedded in a medium with index $n_{med} = 1.33$, such that $\delta n(x,y,z) = 0.08$. The simulations were performed on a grid with $N_x = N_y = N_z = 512$ pixels and a pixel size of $dx = dy = dz = \lambda_{ex}/4 = 92nm$.

In order to analyze the stability of the spatial fluorescence enhancement upon propagation through a scattering medium relative to a homogeneous medium [20], we computed the ratio $\gamma_{scat}/\gamma_{homo}$ of the enhancement factors. γ_{homo} considers the natural beam spreading inherent also in homogeneous space. The change of $\gamma_{scat}/\gamma_{homo}$ over the propagation distance of 47 μm is shown in Fig. 3(c) for a weakly scattering medium with C = 0.1% of beads with radii r = 0.55μm and a strongly scattering medium with C = 2% (same beads). The curves $\gamma_{scat}/\gamma_{homo}$ are averaged from 10 different clusters for a depletion beam with $P_{STED} = 1W, \ell = 3, \alpha = 1.1$. It should be noted that even in the strongly scattering media the maximum decrease of γ_{scat} compared to γ_{homo} is only 35%. Remarkably, this ratio recuperates upon further propagation through the scattering sample, since γ_{scat} and γ_{homo} approach each other while both decay for larger distances z. In this context, but more general, Fig. 3(d) reveals that the effective fluorescence depletion expressed by γ decreases only moderately by 35% and 40% with increasing scattering strength of the medium, expressed by the phase variance $Var[\delta\phi(z)]$. This unintuitive effect, which represents the most important result of the study, is demonstrated for two depletion beams with different linear radial and orbital angular momenta ($\ell = 3, \alpha = 1.1$ and $\ell = 4, \alpha = 1.3$), which have shown to be the optimal beams in the non-scattering case.

5. Light sheet generation in a strongly scattering medium

In order to assess the ability of the STED-MISERB configuration to create a thin light sheet even in a strongly scattering environment, we computed the light sheet fluorescence distribution that is generated by sweeping the illumination and the depletion beam over a field of view with extent 2x_m:

$$F_{LS}(x,y,z) \approx C_{ext}(x,y,z) \cdot Q_{fl} \cdot \frac{1}{2x_m} \cdot \int_{-x_m}^{x_m} \frac{I_{sat} \cdot I_{ex}(x-x_b,y,z)}{I_{sat} + I_{ST}(x-x_b,y,z)} dx_b \qquad (7)$$

The fluorescence distribution, of this novel type of light sheet is compared to the fluorescence generated by a scanned Bessel beam and a scanned Gaussian beam alone. All 3 light sheets were computed for a distribution of randomly placed spheres (r = 0.55μm) with C = 2%. The parameters of the depletion beam were $\ell = 3, \alpha = 1.1$ and $P_{ST} = 5W$. The NA of the Gaussian beam was NA = 0.08 and was chosen such that the lengths of the Gaussian beam and the Bessel beam equal each other.

In order to assess and display the quality of the light sheet, we averaged the fluorescence distribution over the axial range of $2\Delta z \approx 23\mu m$ centered around the peak intensity of each beam: $\bar{F}_{LS,z}(x,y) \approx \frac{1}{2\Delta z} \cdot \int_{z_0-\Delta z}^{z_0+\Delta z} F_{LS}(x,y,z) dz$. The averaged light sheet cross-sections $\bar{F}_{LS,z}(x,y)$ are shown for all 3 illumination modes in Fig. 4(a). Figure 4(b) displays the fluorescence distributions of the static beams in the center of the field of view, again averaged over $2\Delta z$. It can be seen that the STED-MISERB light sheet features the thinnest main peak, even though it also has a weak but broad background compared to the Gaussian beam. While STED-MISERB and Bessel light sheet exhibit smooth average intensity profiles as a result of the self-reconstruction capabilities of the Bessel beams, the average beam profile of the Gaussian beam clearly shows inhomogeneities caused by the scattering medium. This is also highlighted in Fig. 4(c), where the intensity profiles $\bar{F}_{LS,xz}(y)$ give an estimate of the light

sheet thickness. Here $\overline{F}_{LS,xz}(y) \approx \frac{1}{2x_m} \cdot \int_{-x_m}^{x_m} \overline{F}_{LS,z}(x,y)\,dx$ is obtained by the x-projection of $\overline{F}_{LS,z}(x,y)$. The absolute value of the Fourier transform of $\overline{F}_{LS,xz}(y)$ shows that STED-MISERB features the largest amount of spatial frequencies k_y above the cutoff frequency of the Gaussian beam spectrum. This indicates the high axial resolution that can be achieved in 3D imaging even in scattering media using the concept of STED-MISERB: for a cutoff frequency of $k_{y,max} = 10/\mu m$, a so far unreached axial resolution of $\Delta y \approx 2\pi/ k_{y,max} \approx 0.6\mu m$ inside the scattering object is possible. The axial resolutions that can be realized with the convential illumination modes are $\Delta y \approx 0.9\mu m$ for the Bessel light sheet and $\Delta y \approx 1.1\mu m$ for the Gaussian light sheet, indicating a resolution increase for the STED-MISERB light sheet of 33% and 45%, respectively.
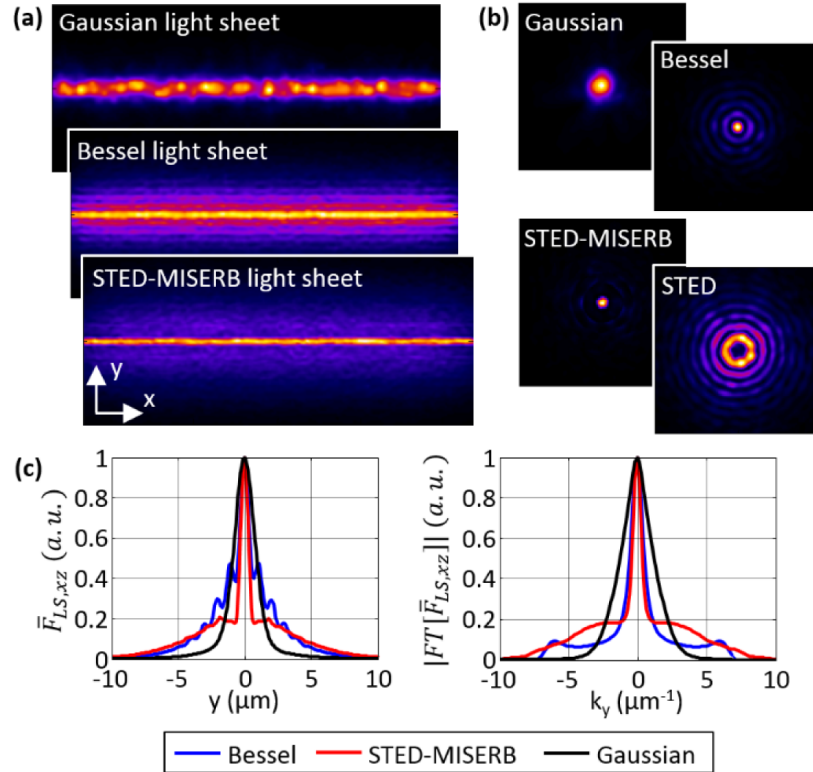
Fig. 4. Spatial extents of light sheets and single beams. (a) Average fluorescence distributions of a Gaussian, Bessel and STED-MISERB light sheet in a scattering medium of beads with r = 0.55µm and C_{Vol} = 2%. The fluorescence distribution is averaged over $2\Delta z \approx 23\mu m$. (b) Averaged single beam profiles of the corresponding beams. (c) xz-projection $\overline{F}_{LS,xz}(y)$ of the light sheets and the corresponding magnitude of its Fourier transform.

6. Summary and conclusions

We have shown by theoretical modelling and computer simulations that it is possible to generate light sheets with superior properties even in inhomogeneous media by the combination of self-reconstructing Bessel beams and the STED principle. The goal in light sheet based microscopy is to excite fluorophores only in a very thin section within an extended, scattering object. However, scattering deteriorates the illuminating wavefront, induces local phase delays, generates strong intensity variations within the illumination beam and thus hinders a smooth, homogeneous, spatially confined fluorescence excitation.

Although it has been shown in earlier studies that Bessel beams reveal a significantly more stable propagation through inhomogeneous media than conventional Gaussian beams [3,31] the efficient application of the STED principle over long propagation distances has been demonstrated only in unrealistic homogeneous media [20], but not in scattering media.

We could show that efficient depletion of fluorophores in the ring system of the Bessel beams by the STED principle results in a very thin and long, needlelike fluorescence distribution even in scattering media. The scattering strength was characterized by the phase variance induced after propagation through the medium. We could achieve an optimal intensity matching of the excitation beam to the STED beam by optimizing the relative radial linear momenta α and the orbital angular momentum ℓ between both Bessel beams. Therefore we had to evaluate quality parameters describing the cross-correlation of both beam intensity distributions. These are on the one hand the overlap $\rho_{diff}(\alpha, \ell)$ between both beams and on the other hand, the spatial fluorescence enhancement $\gamma(\alpha, \ell)$, expressing the fluorescence depletion in the ring system relative to the fluorescence in the beam center. Different to conventional STED using point-scanning applied in weakly scattering objects, in our study the quality factors $\gamma(\alpha, \ell)$, and $\rho_{diff}(\alpha, \ell)$ have to remain nearly invariant along a beam propagation distance of 50 μm in strongly scattering media. By BPM simulations we found that the optimal radial and angular orbital beam momenta obtained for the homogeneous case can be transferred to apply the STED principle also in various scattering media.

This remarkable result expresses that despite significant local phase delays in each beam, the global phase difference between both beams is sufficiently small to deplete the fluorescence efficiently in the ring system, but hardly in the beam center. Depending on the depletion beam, the effective depletion expressed by γ, decays by less than 35% or 40% respectively after 50μm propagation of two Bessel beams through an inhomogeneous medium, which can deteriorate the beam profile of conventional Gaussian beams significantly. We believe that our study helps to better understand the propagation behavior of phase modulated waves in inhomogeneous media and thereby to design novel types of light sheet microscopes.